QUBIC III: Laboratory Characterization

S A Torchinsky, J.-Ch Hamilton, M. Piat, E S Battistelli, C Chapron, G d'Alessandro, P de Bernardis, M de Petris, M M Gamboa Lerena, M Gonzalez, et al.

HAL Id: hal-02999031

https://hal.science/hal-02999031

Preprint submitted on 10 Nov 2020

QUBIC III: Laboratory Characterization

S.A. Torchinsky[1,2] **J.-Ch. Hamilton**[1] **M. Piat**[1] **E.S. Battistelli**[3,4]
C. Chapron[1] **G. D'Alessandro**[3,4] **P. de Bernardis**[3,4] **M. De Petris**[3,4]
M.M. Gamboa Lerena[5,6] **M. González**[7] **L. Grandsire**[1] **S. Marnieros**[8]
S. Masi[3,4] **A. Mennella**[9,10] **L. Mousset**[1] **J.D. Murphy**[11]
C. O'Sullivan[11] **D. Prêle**[1] **G. Stankowiak**[1] **A. Tartari**[12]
J.-P. Thermeau[1] **F. Voisin**[1] **M. Zannoni**[13,14] **P. Ade**[15] **J.G. Alberro**[16]
A. Almela[17] **G. Amico**[3] **L.H. Arnaldi**[7] **D. Auguste**[8] **J. Aumont**[18]
S. Azzoni[19] **S. Banfi**[13,14] **B. Bélier**[20] **A. Baù**[13,14] **D. Bennett**[11]
L. Bergé[8] **J.-Ph. Bernard**[18] **M. Bersanelli**[9,10] **M.-A. Bigot-Sazy**[1]
J. Bonaparte[21] **J. Bonis**[8] **E. Bunn**[22] **D. Burke**[11] **D. Buzi**[3]
F. Cavaliere[9,10] **P. Chanial**[1] **R. Charlassier**[1] **A.C. Cobos Cerutti**[17]
F. Columbro[3,4] **A. Coppolecchia**[3,4] **G. De Gasperis**[23,24]
M. De Leo[3,25] **S. Dheilly**[1] **C. Duca**[17] **L. Dumoulin**[8] **A. Etchegoyen**[17]
A. Fasciszewski[21] **L.P. Ferreyro**[17] **D. Fracchia**[17] **C. Franceschet**[9,10]
K.M. Ganga[1] **B. García**[17] **M.E. García Redondo**[17] **M. Gaspard**[8]
D. Gayer[11] **M. Gervasi**[13,14] **M. Giard**[18] **V. Gilles**[3,26]
Y. Giraud-Heraud[1] **M. Gómez Berisso**[7] **M. Gradziel**[11]
M.R. Hampel[17] **D. Harari**[7] **S. Henrot-Versillé**[8] **F. Incardona**[9,10]
E. Jules[8] **J. Kaplan**[1] **C. Kristukat**[27] **L. Lamagna**[3,4] **S. Loucatos**[1,28]
T. Louis[8] **B. Maffei**[29] **W. Marty**[18] **A. Mattei**[4] **A. May**[26]
M. McCulloch[26] **L. Mele**[3,4] **D. Melo**[17] **L. Montier**[18] **L.M. Mundo**[16]
J.A. Murphy[11] **F. Nati**[13,14] **E. Olivieri**[8] **C. Oriol**[8] **A. Paiella**[3,4]
F. Pajot[18] **A. Passerini**[13,14] **H. Pastoriza**[7] **A. Pelosi**[4] **C. Perbost**[1]
M. Perciballi[4] **F. Pezzotta**[9,10] **F. Piacentini**[3,4] **L. Piccirillo**[26]
G. Pisano[15] **M. Platino**[17] **G. Polenta**[3,30] **R. Puddu**[31] **D. Rambaud**[18]
E. Rasztocky[32] **P. Ringegni**[16] **G.E. Romero**[32] **J.M. Salum**[17]
C.G. Scóccola[5,6] **A. Schillaci**[3,33] **S. Scully**[11,34] **S. Spinelli**[13]
M. Stolpovskiy[1] **A.D. Supanitsky**[17] **P. Timbie**[35] **M. Tomasi**[9,10]
G. Tucker[36] **C. Tucker**[15] **D. Viganò**[9,10] **N. Vittorio**[23] **F. Wicek**[8]
M. Wright[26] **and A. Zullo**[4]

[1]Université de Paris, CNRS, Astroparticule et Cosmologie, F-75006 Paris, France

²Observatoire de Paris, Université Paris Science et Lettres, F-75014 Paris, France

³Università di Roma - La Sapienza, Roma, Italy

⁴INFN sezione di Roma, 00185 Roma, Italy

⁵Facultad de Ciencias Astronómicas y Geofísicas (Universidad Nacional de La Plata), Argentina

⁶CONICET, Argentina

⁷Centro Atómico Bariloche and Instituto Balseiro (CNEA), Argentina

⁸Laboratoire de Physique des 2 Infinis Irène Joliot-Curie (CNRS-IN2P3, Université Paris-Saclay), France

⁹Università degli studi di Milano, Milano, Italy

¹⁰INFN sezione di Milano, 20133 Milano, Italy

¹¹National University of Ireland, Maynooth, Ireland

¹²INFN sezione di Pisa, 56127 Pisa, Italy

¹³Università di Milano - Bicocca, Milano, Italy

¹⁴INFN sezione di Milano - Bicocca, 20216 Milano, Italy

¹⁵Cardiff University, UK

¹⁶GEMA (Universidad Nacional de La Plata), Argentina

¹⁷Instituto de Tecnologías en Detección y Astropartículas (CNEA, CONICET, UNSAM), Argentina

¹⁸Institut de Recherche en Astrophysique et Planétologie, Toulouse (CNRS-INSU), France

¹⁹Department of Physics, University of Oxford, UK

²⁰Centre de Nanosciences et de Nanotechnologies, Orsay, France

²¹Centro Atómico Constituyentes (CNEA), Argentina

²²University of Richmond, Richmond, USA

²³Università di Roma "Tor Vergata", Roma, Italy

²⁴INFN sezione di Roma2, 00133 Roma, Italy

²⁵University of Surrey, UK

²⁶University of Manchester, UK

²⁷Escuela de Ciencia y Tecnología (UNSAM) and Centro Atómico Constituyentes (CNEA), Argentina

²⁸IRFU, CEA, Université Paris-Saclay, F-91191 Gif-sur-Yvette, France

²⁹Institut d'Astrophysique Spatiale, Orsay (CNRS-INSU), France

³⁰Italian Space Agency, Roma, Italy

³¹Pontificia Universidad Catolica de Chile, Chile

³²Instituto Argentino de Radioastronomía (CONICET, CIC, UNLP), Argentina

³³California Institute of Technology, USA

³⁴Institute of Technology, Carlow, Ireland

³⁵University of Wisconsin, Madison, USA

³⁶Brown University, Providence, USA

E-mail: satorchi@apc.in2p3.fr, hamilton@apc.in2p3.fr, piat@apc.univ-paris7.fr

Abstract.   A prototype version of the Q & U Bolometric Interferometer for Cosmology (QUBIC) underwent a campaign of testing in the laboratory at Astroparticle Physics and

Cosmology in Paris. We report the results of this Technological Demonstrator which successfully shows the feasibility of the principle of Bolometric Interferometry. Characterization of QUBIC includes the measurement of the synthesized beam, the measurement of interference fringes, and the measurement of polarization performance. A modulated and frequency tunable millimetre-wave source in the telescope far-field is used to simulate a point source. The QUBIC pointing is scanned across the point source to produce beam maps. Polarization modulation is measured using a rotating Half Wave Plate. The measured beam matches well to the theoretical simulations and gives QUBIC the ability to do spectro imaging. The polarization performance is excellent with less than 0.5% cross-polarization rejection. QUBIC is ready for deployment on the high altitude site at Alto Chorillo, Argentina to begin scientific operations.

Contents

1 Introduction

The detection of B-mode polarization in the Cosmic Microwave Background (CMB) is the subject of a worldwide effort due to its importance as a confirmation of the Inflationary model of Cosmology. A clear detection of polarization B-modes in the CMB is evidence of primordial gravitational waves expected during the inflationary phase in the earliest moments of the Universe. For an overview see [1].

Polarization in the CMB is expected to be a small fraction of the CMB signal itself while the B-mode component of polarization will be several orders of magnitude smaller again. As a result, the measurement of B-mode polarization is a difficult exercise of extracting a signal buried deep within other signals (the CMB E-mode but also foreground contamination and lensing) and noise. This requires very careful instrument design and implementation, with sophisticated data analysis to separate unwanted contributions from the B-mode signal.

The Q and U Bolometric Interferometer (QUBIC) is designed with particular attention to the limitation and control of systematics [2]. See also in this series of papers [3] for the optics design, [4] for the cryogenics design, and [5] for the readout electronics. QUBIC uses the technique of interferometry which leads to the possibility of doing "self-calibration" in order to have exquisite control of instrument systematics [6]. This technique also provides a method for doing spectral imaging. Bolometric Interferometry is the marriage of techniques bringing together the great sensitivity and large bandwith of bolometers and the instrumental control and high fidelity imaging of aperture synthesis. Using this innovative approach, any residual systematics in the data will be largely independent from those in other experiments, thus providing a uniquely powerful dataset in the context of the worldwide experimental effort.

An imaging interferometer measures "visibilities" which are the complex (amplitude and phase) correlations between each antenna pair (baseline). In radio astronomy, the visibilities are recorded directly. A "correlator" digitizes the signals and multiplies pairs of signals to

produce a stream of complex numbers, each of which corresponds to the cross correlation product of an antenna-pair. Channelization of the bandpass permits signal processing of individual, very narrow bands, and for each channel the signal is nearly monochromatic. In radio astronomy, large bandwidths are achieved by adding more digital electronics.

A bolometric interferometer takes advantage of the high sensitivity and large bandwidth of bolometers while also benefitting from the calibration technique possible with an imaging interferometer. The spatial sampling of the sky is generated by placing a cluster of back-to-back horns that behave effectively as electromagnetic nozzles. This horn cluster creates the $u - v$ sampling of the aperture plane equivalent to what is done by a distribution of antennas in a radio array. For the bolometric interferometer, instead of sampling the signals and computing the cross correlations between antenna pairs, the interference pattern is imaged.

A single image of the interference pattern has all the information convolved together resulting in observing the sky through a synthesized beam. The shape of this synthesized beam is given by the combination of all individual baselines (all pairs of horns). The bolometric interferometer end up being a synthesized imager observing the sky through its synthesized beam just the same way as a classical imager observes the sky through the beam formed by the telescope. For calibration and instrumental systematics studies it is however crucial to extract the individual visibilities. By blocking all horns except two, we measure the interference pattern of that baseline [see 6]. For example, using a 20×20 cluster of horns as in the QUBIC Final Instrument (QUBIC-FI), there are 400 horns making $n(n-1)/2 = 79800$ baselines which are needed to be observed individually for self-calibration. The QUBIC Technological Demonstrator (QUBIC-TD) under test in the lab at APC has a smaller horn array with only 64 horns in a square array giving 2016 baselines.

Performance of the bolometric interferometer improves as the number of baselines increases. A larger cluster of horns provides more baselines, but this in turn must be sampled by a larger array of detectors in the focal plane. As a result, the overall sensitivity of the bolometric interferometer is indirectly a function of the number of detectors in so much as the focal plane must be large enough to match the horn cluster.

An additional feature of bolometric interferometry is the ability to do spectroimaging. The synthesized beam varies with frequency [for details see 3]. In particular, the beam secondary lobes move inward as frequency increases while the central lobe remains in the same place. As a result, the Time Ordered Data effectively samples different frequencies as the beam passes over the same point in the sky. This frequency selectivity can be deconvolved in the data post processing. The spectral resolution improves with the number of baselines as the synthesized beam has finer secondary lobes with a larger cluster of horns. Spectroimaging is an innovative feature of bolometric interferometry which gives QUBIC an important advantage over other CMB imagers [see 7, 8, for details] and the possibility to do this with QUBIC has been confirmed (see Section 7).

This paper is organized as follows. The laboratory setup is described in Section 2 with particular attention given to the placement and alignment of the calibration source. Section 3 presents the measured bandpass of QUBIC. Section 4 shows the measured response to modulated polarization using the rotating Half Wave Plate. The QUBIC design provides extremely pure polarization performance with 99.9% cross polarization rejection. Section 5 shows the measurement of fringes on the focal plane using the mechanical switches in the horn array to select baselines. Section 6 shows an early application of self testing with the independent determination of the physical orientation of the horn array using the fringe measurements. In Section 7 we show measurements of the QUBIC synthesized beam, and

in Section 8 we demonstrate the results of the QUBIC mapmaking pipeline by generating a "sky" map of the calibration source using the calibration information determined from previous measurements. Finally, some concluding remarks are given in Section 9.

2   Calibration Source Setup

Characterization of the QUBIC instrument is done primarily using a frequency tunable monochromatic point source in the far-field. This permits measurement of the bandpass (Section 3), the polarization performance (Section 4), the measurement of interference fringes (Section 5 and Section 6), and the beam Point Spread Function (PSF - Section 7 and Section 8). This section describes the optical setup used to characterize QUBIC.

The setup is shown in the sketch of Figure 1. The calibration source points at a flat mirror which redirects the beam into the QUBIC cryostat window. There is an 11 m optical path, putting the calibration source comfortably in the far field.
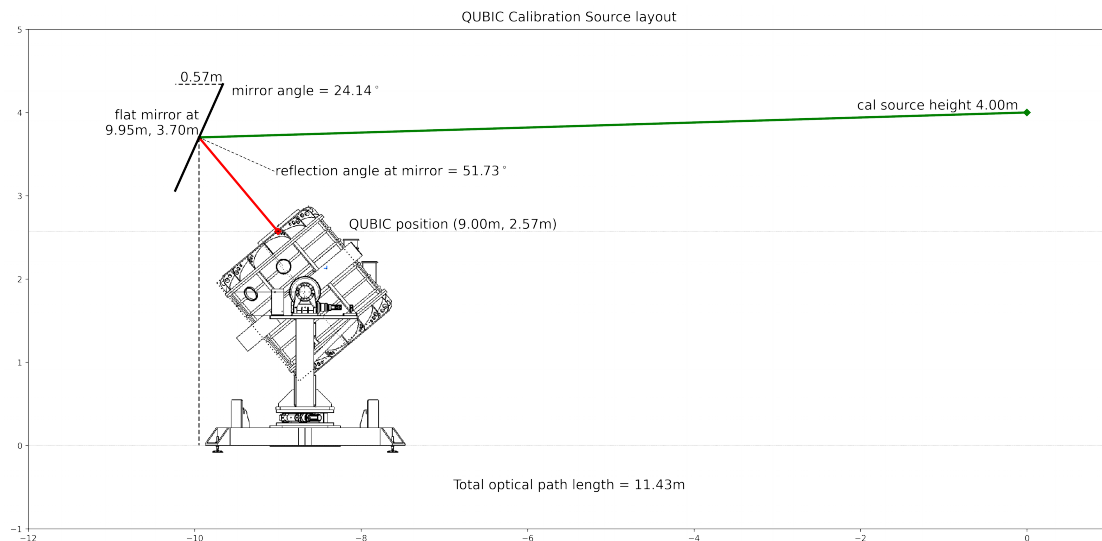
Figure 1. Layout for the calibration source relative to the QUBIC instrument.

The flat mirror is an aluminium sheet mounted on a scaffolding at a height of 3.5 m (photo in Figure 2). The tilt angle of the flat mirror can be adjusted by a long screw permitting very precise selection for the correct tilt angle.

Alignment of the system was accomplished using a laser temporarily mounted at the window of the QUBIC cryostat, pointing normal to the window (photo Figure 3). The laser light is reflected from the flat mirror to the calibration source where a small flat mirror was fitted to the front of the calibration source feedhorn. The laser reflects from the mirror at the feedhorn mouth and returns to the large flat mirror and finally to the QUBIC cryostat window. In the photo (Figure 3), one can clearly see the spot of the laser on the corner of the laser mounting structure on the window. The alignment is therefore precise to within a fraction of a degree which is well within the tolerance necessary to have the calibration source visible to the QUBIC-TD.

The calibration source system is composed of a number of electronics aside from the source itself. The calibration source was purchased from VDI electronics and is composed of

Figure 2. **left:** Photo of QUBIC looking along the line-of-sight from the calibration source. The reflection of the window is clearly visible in the flat mirror. **right:** The flat mirror is mounted on a scaffold at a height of 3.5 m and has a finely adjustable tilt angle using a system composed of a long screw.

a Gunn oscillator running at frequencies around 10 GHz. Two multipliers in a chain follow the synthesiser multiply the base frequency by 12 resulting in frequencies around 150 GHz. The range of the system is between 130 GHz and 170 GHz. The source can be commanded via USB connection to select the frequency. This is done by a nearby Raspberry Pi mini computer (see photo Figure 4).

A signal generator provides a square wave at around 1 Hz which is used to modulate the calibration source. The Raspberry Pi configures the signal generator, selecting the amplitude, offset, frequency, shape, and duty cycle.

The power output from the calibration source is monitored at a port near the calibration source feedhorn which provides a voltage which is a function of the output power. This voltage is sent to an Analog-to-Digital Converter (ADC) board integrated in the Raspberry Pi mini computer which stores the data along with a timestamp for each sample. There are approximately 300 samples per second.

A Command Line Interface written in python is used to configure the calibration source setup. This system accepts commands via socket and can be easily interfaced by the Graphical User Interface called QubicStudio.

For the result shown in Figure 5, the source was set at 150 GHz and was modulated with a square wave with 3 second period (0.333 Hz) and a 33% duty cycle. Figure 5 shows the very clear signal in many of the TES detectors in the array. Figure 6 shows the signal
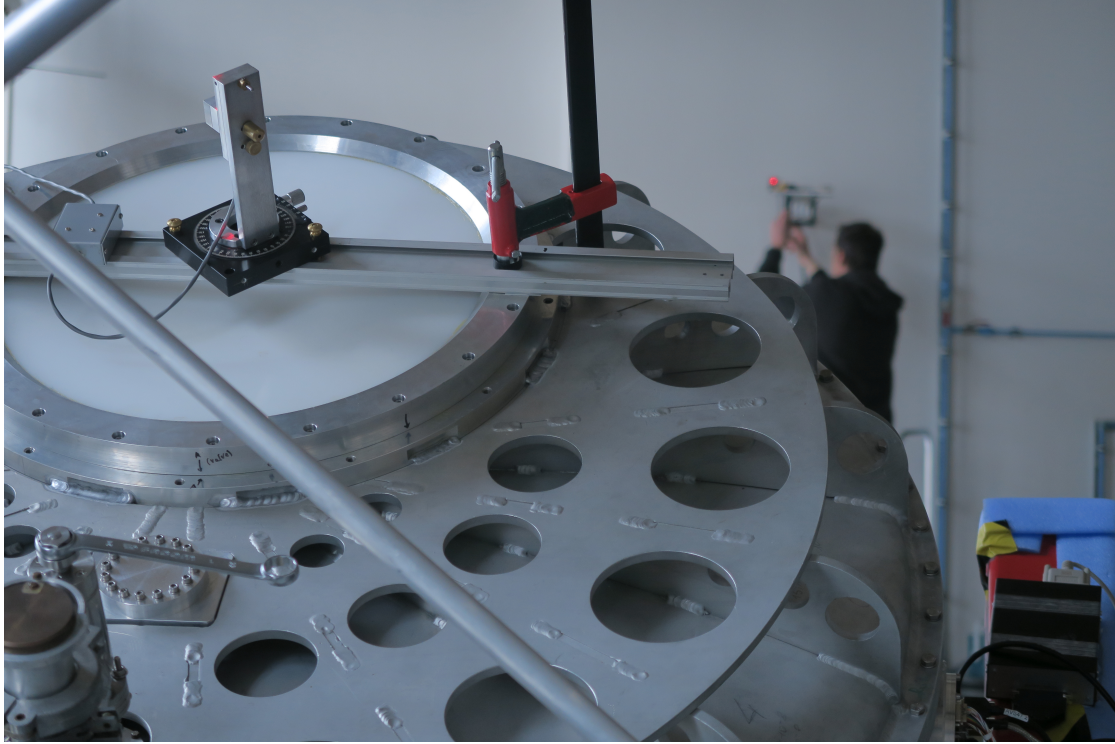
Figure 3.   Photo of the alignment procedure. The laser is mounted orthogonal to the cryostat window and shines towards the flat mirror, sending the light to the calibration source feedhorn at the other side of the room. A small mirror fitted to the mouth of the feedhorn sends the laser light back on the same path to the cryostat window. The laser spot is clearly visible on the laser mount structure.

seen on one TES together with the modulation signal measured by the power monitor. There is a very clear correlation between the two.
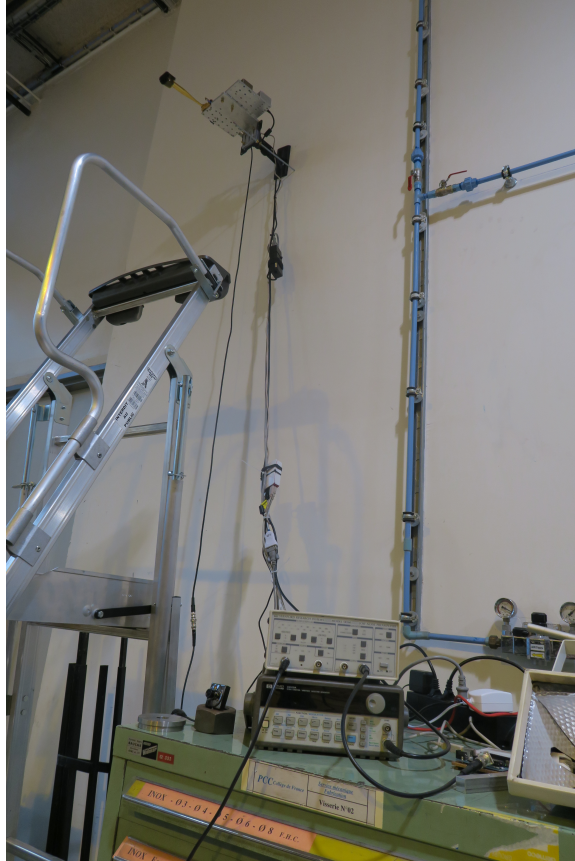
Figure 4. Photo of the electronics associated with calibration source setup. This includes a signal generator for modulating the calibration source with a square wave. The output power of the calibration source is sent through an amplifier and then digitized by an ADC board integrated in the Raspberry Pi (seen suspended on the cables below the calibration source).
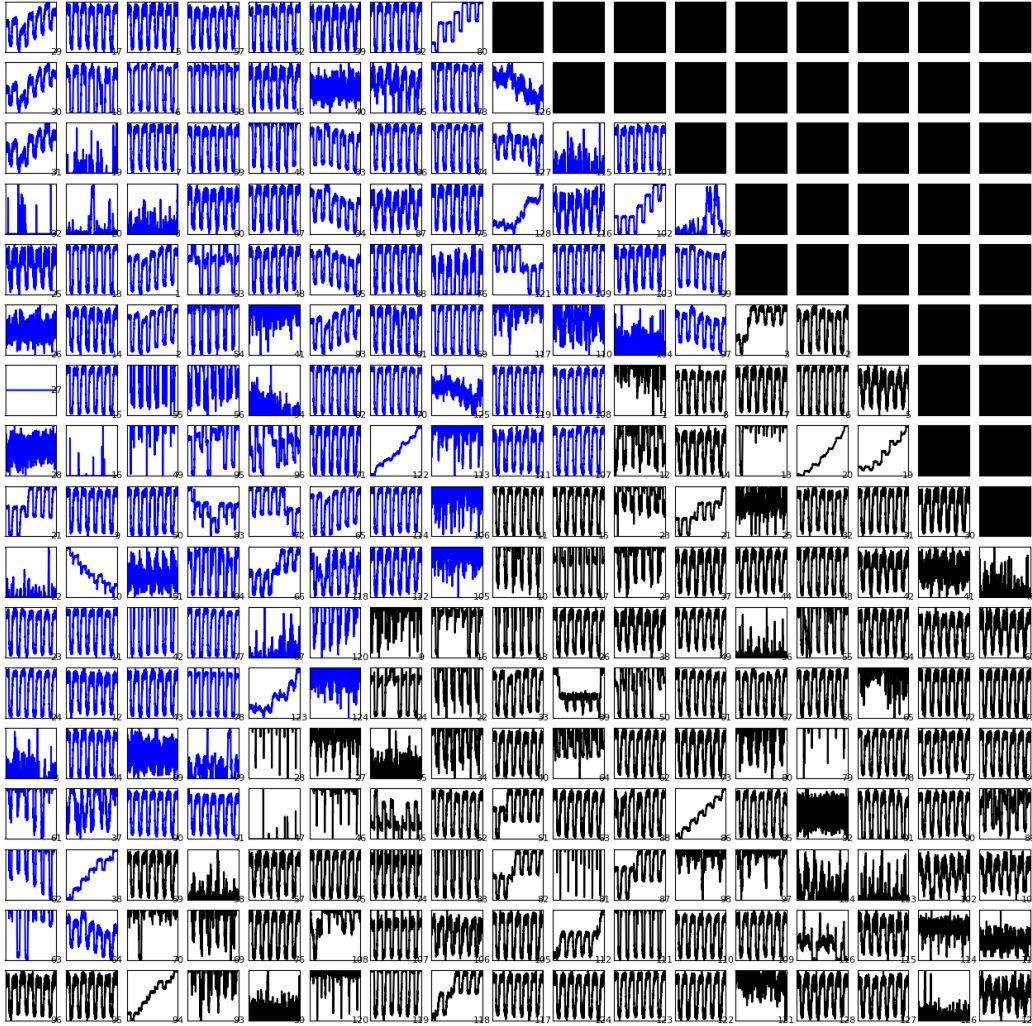
Figure 5. The first measurement of the calibration source by QUBIC. The signal is clearly seen in most pixels, corresponding to the good pixels in the array [see 5, for a discussion on the bolometer array performance]. The black "pixels" in the top-right are empty positions. The QUBIC Final Instrument will have four arrays equivalent to this one in order to make a roughly circular focal plane for each frequency channel.
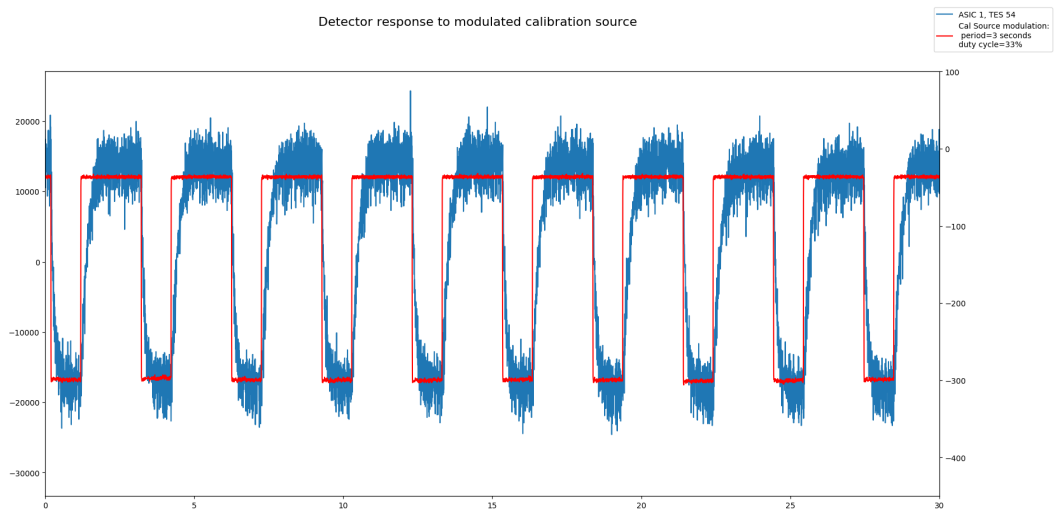
Figure 6. Overlay of the signal detected by TES#54 of the QUBIC array (blue curve) together with the modulated calibration source signal as measured by the calibration source power monitor (red curve).

3 Spectral Response

The spectral response was measured using the calibration source (see Section 2). The calibration source was setup with a sine wave modulation at 1 Hz and stepped through frequencies across the band from 110 GHz to 180 GHz. After synchronized demodulation at the bolometer, this provides an extremely high signal-to-noise measurement. Figure 7 shows the measured profile which corresponds to the expected profile of the filter provided by Cardiff. The plot shows the average of all operational TES [181 detectors, see 5], as well as the median, and the points filtered for minimum 3σ detection. All curves agree within the bandpass.
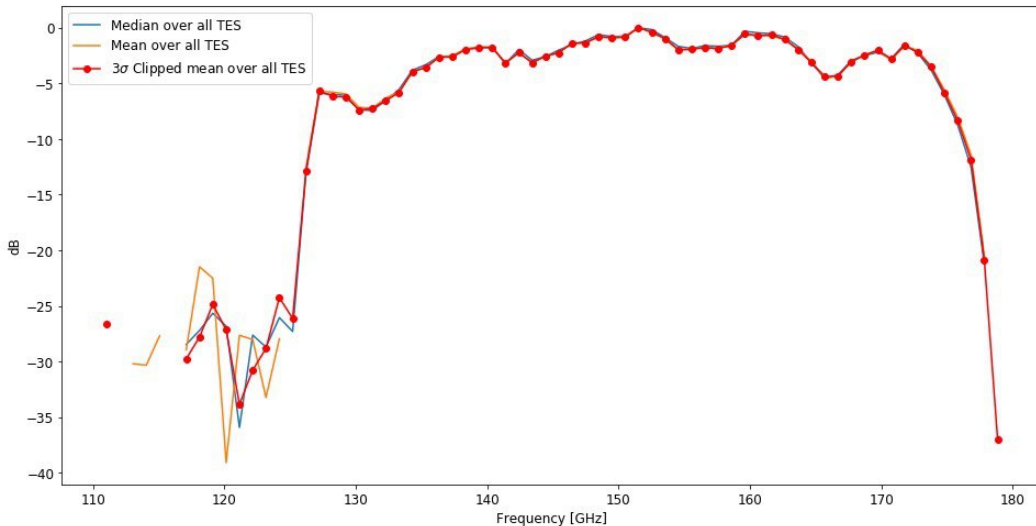
Figure 7. Bandpass of the QUBIC Technological Demonstrator. This was measured by stepping through the frequencies of the calibration source and measuring the relative power on the TES at each frequency.

4 Half Wave Plate Polarization Rotation Test

A functionality test was carried out of the Half Wave Plate rotator mechanism, and at the same time, the calibration source was operating. Measurements were taken at each of the 7 evenly spaced positions of the Half Wave Plate from 0° to 90° (spacing of 15°).

Figure 8 shows the signal, after Fourier filtering, for TES #95 at the different HWP positions. The peak-to-peak amplitude clearly varies with HWP position. Each position is shown in a different colour. Figure 9 shows a zoom of the calibration source signal measured by TES#95 with the HWP in position #1. The amplitude at each position is plotted and fitted to a sine curve, as shown in Figure 10.

The cross-polarization contamination at 150 GHz is compatible with zero to within 0.18%. The signal in each case was measured by the RMS of the TES data in a given position while the source was modulated. The measurement was the source modulation amplitude together with the RMS of the noise, quadratically added. As a result the minimum value is dominated by noise. The maximum signal occurs when the HWP is between position 6 and 7.

As polarization is selected before the horn array, the cross-polarization leakage is independent of the location in the focal plane. Therefore, the cross-polarization leakage is
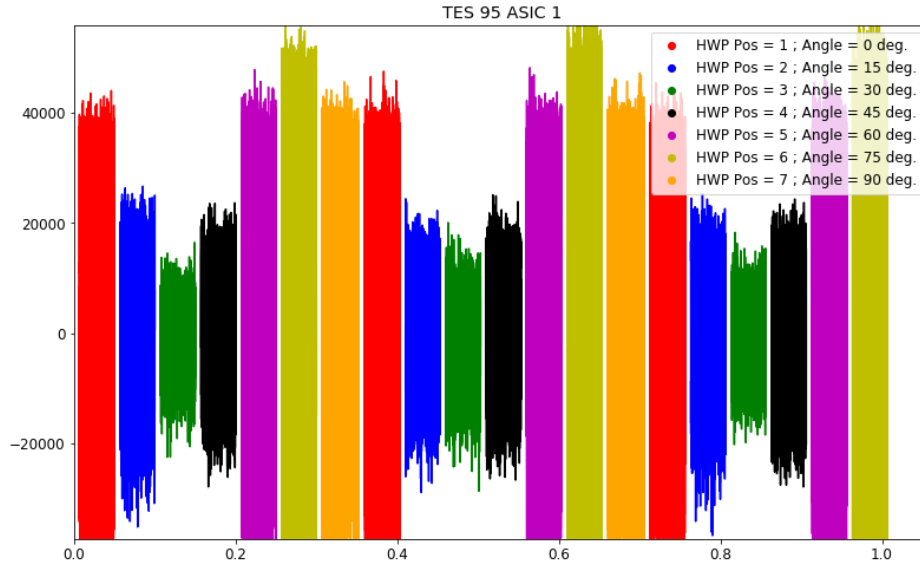
Figure 8. Peak-to-peak amplitude of the detected calibration source for different Half Wave Plate positions as measured with TES#95
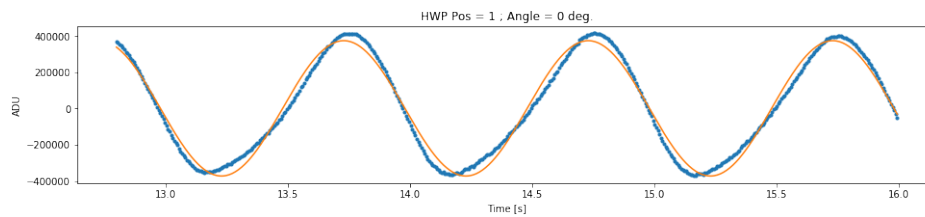

Figure 9. Peak-to-peak amplitude of the detected calibration source for the Half Wave Plate in position #1 as measured with TES#95. The blue curve is the response measured by the bolometer and the orange curve is the power monitor of the calibration source (see Section 2).
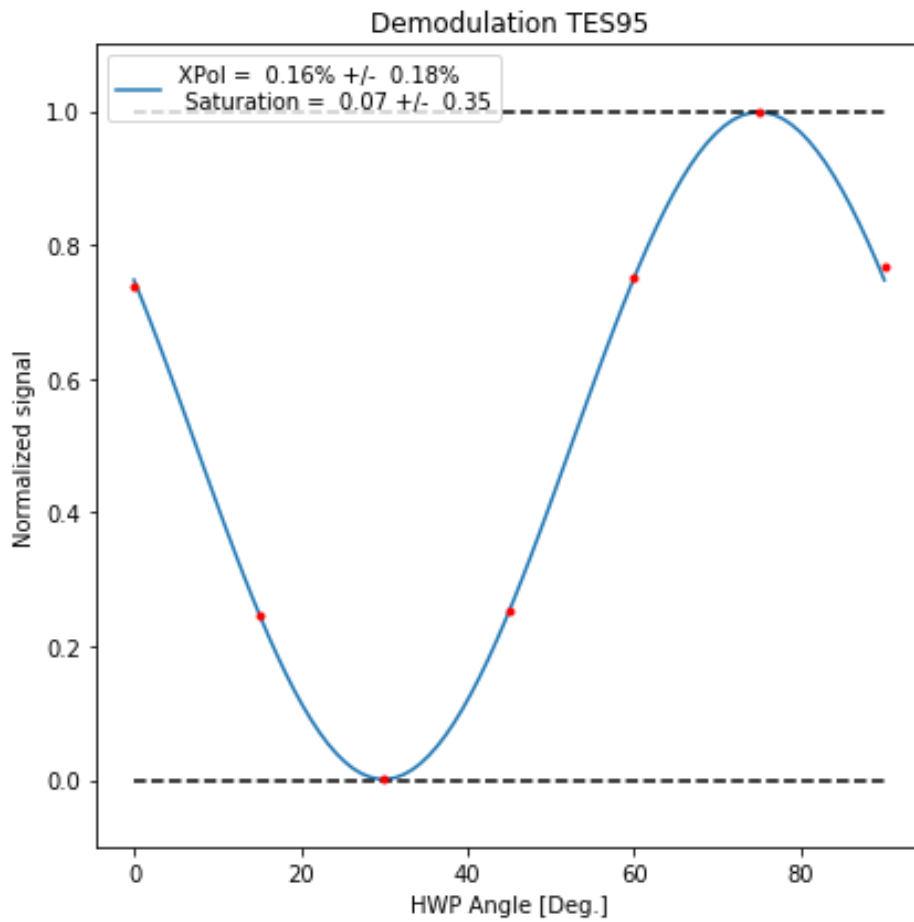
Figure 10. Amplitude of the detected calibration source at 150 GHz as measured with TES#95 for the Half Wave Plate in the different positions and fitted to a sine curve.
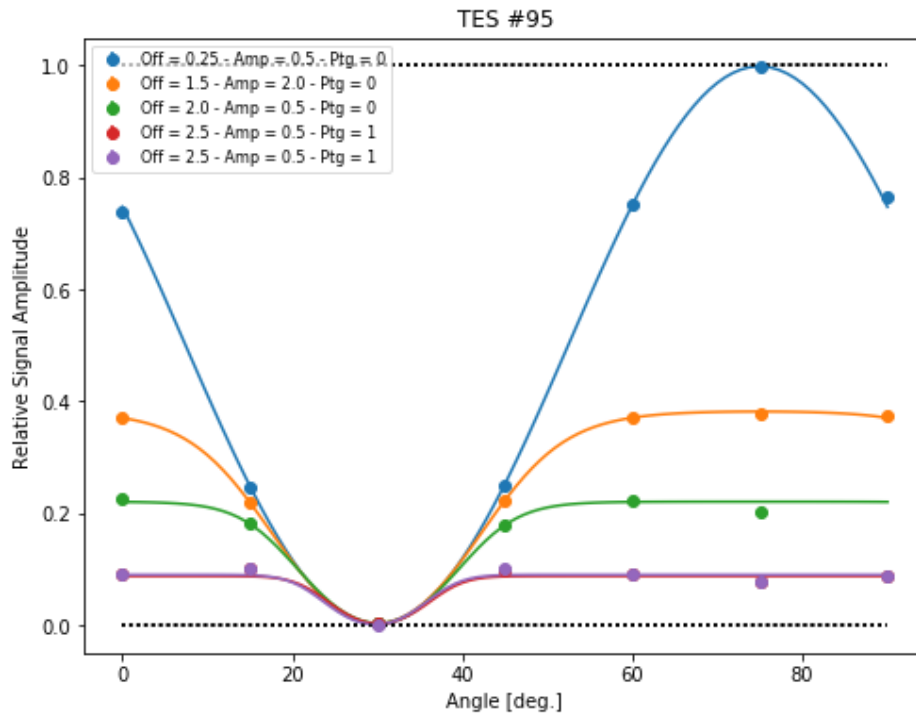
Figure 11. Same as Figure 10 but with the calibration source set at various power output levels. The effect of saturation is evident for the source at high power. The Half Wave Plate angle of maximum signal damping is consistent between all the measurements.
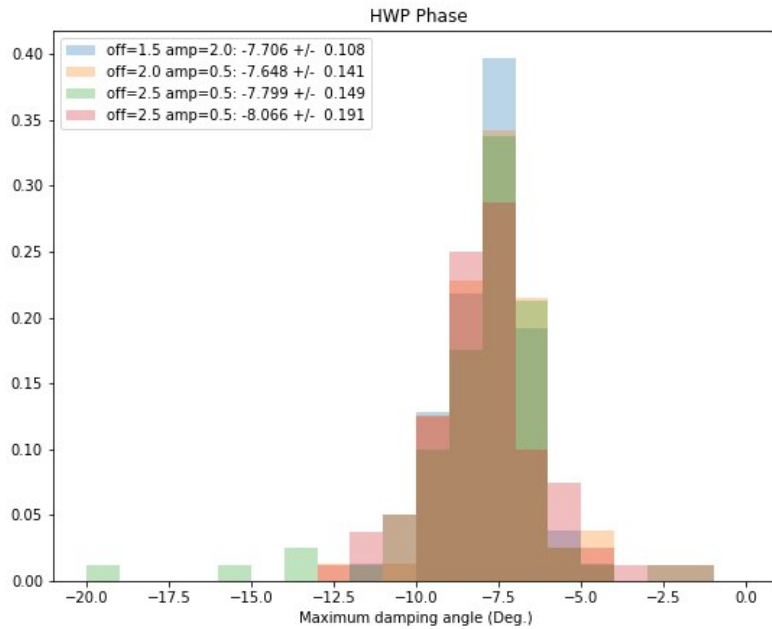
Figure 12. Distribution of the trough in the amplitude for various source output power (see Figure 11).

expected to be the same for all TES. The example shown in Figures 10 and 11 are for TES#95 which has the best signal-to-noise for this measurement due to the pointing.

The measured cross-polarization contamination was measured with the calibration source tuned to 150 GHz. This is therefore a measurement at a single, essentially monochromatic frequency. Future measurements will measure the cross-polarization contamination at frequencies across the band in order to determine the integrated response of the system for the full bandpass.

5 Self-Calibration

Self Calibration is a technique developed for aperture synthesis in radio interferometry. This technique evolved from the original idea in the 1970's of "phase-closure" [9–11] to become in the early 1980's "self-calibration" [12, 13]. See [14] for a detailed overview. Precise knowledge of the calibration source is not required, as long as it is a strong and stable point source. The large number of baseline visibilities allows us to solve for many unknowns, including the gain and phase corrections required, without having knowledge of the source amplitude.

In order to advance towards the full analysis of self-calibration, a key component is the ability to measure fringes with QUBIC. If fringes can be measured with a horn pair, then the full analysis can be done once the fringe measurement is done for all horn pairs. By measuring the fringe pattern of a single pair of horns we demonstrate the feasibility of doing self-calibration with the bolometric interferometer.

The QUBIC Technological Demonstrator successfully measured fringes between a pair of horns (Figure 13 left). This is the derived image after analysing measurements of images with all horns open, with two horns closed, with one horn closed, and with the other horn closed. This is the equivalent of having all horns closed except the two, as shown in [6]. The fringes are expected to be fainter in proportion to the distance to the centre of the focal plane (Figure 13 right). This is not the case here because of saturation of the TES detectors. As a result, the fringe amplitude appears to be relatively constant, or near zero where saturated detectors were subtracted from one another. The problem with saturation was due to the cryogenic system which did not reach the optimum temperature for the TES. Future tests will work below the saturation point of the TES.
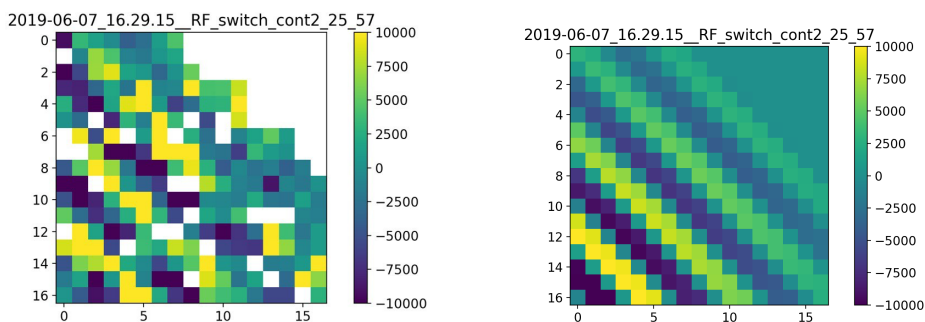

Figure 13. **left:** Fringes measured on the QUBIC TES array. Fringes are clearly visible as bright, diagonal lines across the detector array. **right:** Simulation of the fringe pattern expected to be measured with a baseline between horns 25 and 57. The fringe lines are in the same place as the measured image (left). The amplitude of the fringe lines are fainter with distance from the centre of the focal plane. This was not measured because of saturation of the detectors.

An initial analysis using the fringe measurement is carried out in Section 6. The measurement is used to verify the orientation of the horn array.

6 Verification of the Horn Cluster Orientation with Fringe Measurements

The orientation and spacing of the fringe pattern seen in the focal plane is a function of the selected baseline which is determined by which horns are open or closed. In this section, we describe the use of the fringe measurement at different baselines to confirm the mechanical orientation of the horn cluster.

The fringe pattern described in the previous section was measured for the baseline formed by horns 25-57 (see Figure 13 above). The position of the horn cluster at that time was verified using pictures taken when it was mounted (see Figure 14). Figure 15 shows the
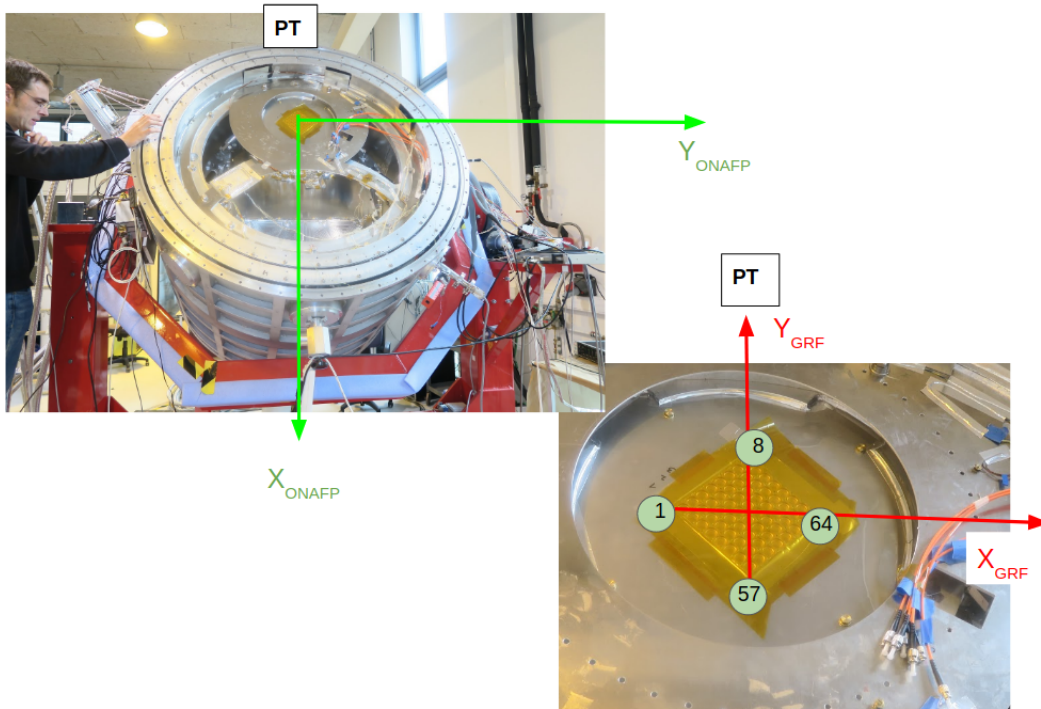
Figure 14. Pictures showing the the horn cluster orientation. **left:** The On Axis Focal Plane (ONAFP) reference frame projected onto the face of the horn cluster. **right:** The Global Reference Frame (GRF) is co-planar to the face of the horn cluster.

reference frames used on the instrument.

Simulations of interferometry patterns obtained on the focal plane for different horn configurations are done using geometric optics and calculating the interference at infinity. This is computed as if the horn plane and the focal plane were parallel. Simulations are also performed in Maynooth with `GRASP` (a commercial optical modelling software) and `MODAL` (an 'in-house' software developed and maintained by Marcin Gradziel at Maynooth) [see 3, for details about optics modelling]. While both software packages model systems using the technique of Physical Optics, there are differences in how systems are implemented which make them complementary. `MODAL` can calculate the coupling of beams from free-space to feedhorns, while `GRASP` considers feedhorns to be point sources. However, `GRASP` can describe
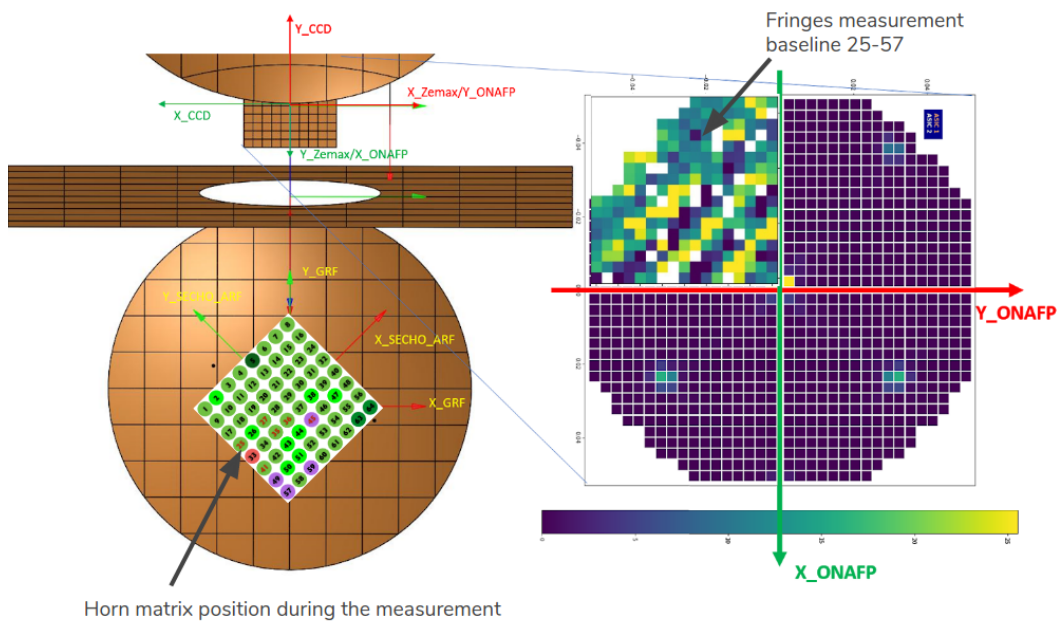
Figure 15. QUBIC reference frames. **left:** The face of the horn cluster is overlaid on the optics schematic. **right:** The fringe measurement in the negative-x and negative-y quadrant (quadrant 3).

surfaces using a grid of points which permits the modeling of real measured mirror surfaces, and then using the Physical Theory of Diffraction, `GRASP` can model mirror edge effects. The two packages can exchange data through common file formats which permits the analysis of a complete optical system, using the best package for each subsystem and then combining the results. They can also be used independently and compared as a verification of modelling results.

A model was created in `GRASP` to match the `MODAL` model. This model plots the interference pattern of any horn baseline. The comparison of the output of the models for a given baseline is shown in Figure 16 as plotted by our Python-based QUBIC simulation software using the output files from the `MODAL` simulation model. The result shows that `MODAL` and the `GRASP` simulations are in agreement. Additional baselines were tested and also had matching patterns. Having these two independent methods in agreement is a good check that the horn setup, instrument data, software, and simulations are working as expected.
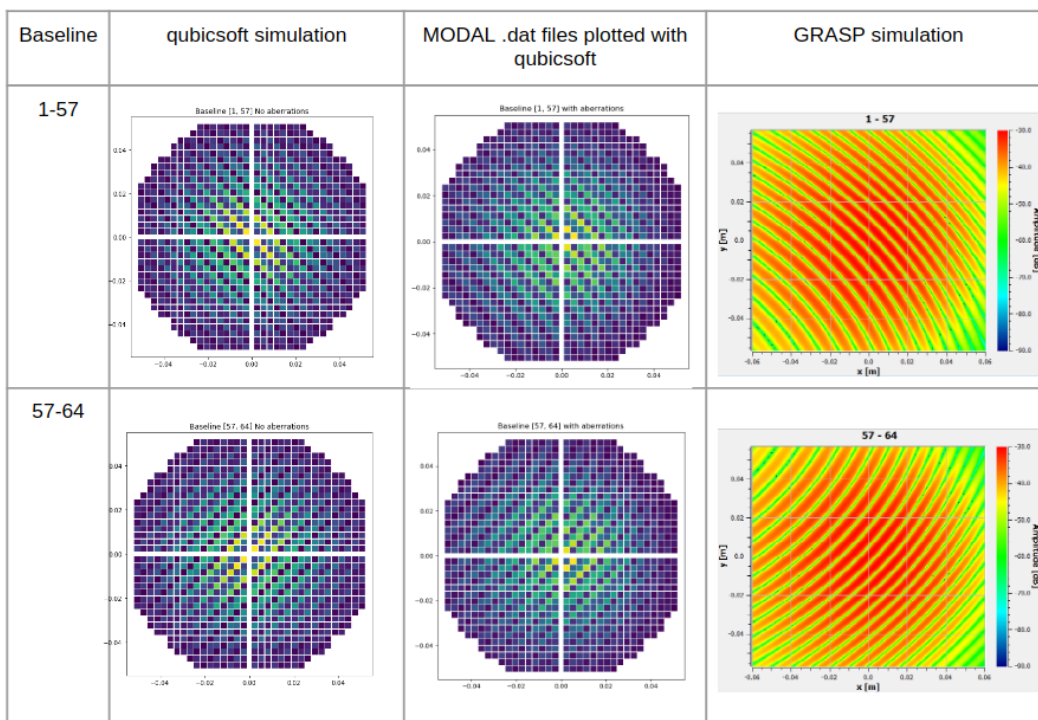
Figure 16. Fringes obtained on the focal plane for given baselines using our Python-based QUBIC simulation software (optical geometry) using results from the `MODAL` simulatin. The corresponding `GRASP` simulation is shown on the right.

Finally, the optics simulations can be used to confirm the physical horn orientation in the optical path. The orientation between all the simulations and the measurement agree. A $\pi/2$ rotation difference between measured results and simulations would be easily detected. However, it is not straightforward to detect a π rotation because the differences would be very small (see Figure 17). Such a rotation might be detectable by fitting the measurement with the simulations from Maynooth, and is a work in progress.

The main concern which motivated this study was to confirm that the horn switch electronics [15] was operating the switches as expected. That is, that the horn commanded to be open or closed was in the correct physical location in the horn cluster. This was confirmed.
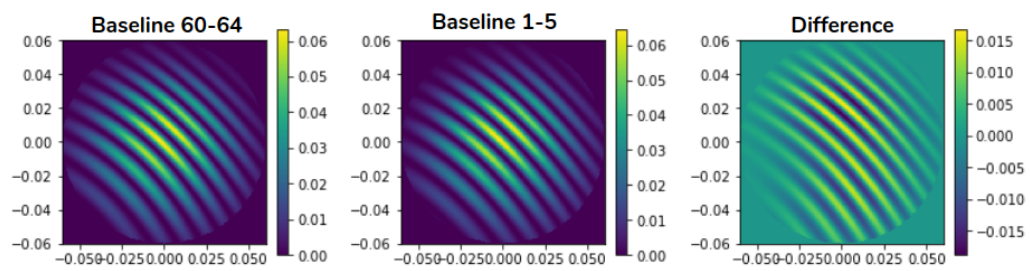
Figure 17. Fringes obtained on the focal plane for 2 baselines, symmetric under a π rotation.

7 Synthetic full Beam reconstruction

The QUBIC-TD synthetic beam maps were measured at five frequencies in the range 130 GHz to 170 GHz by tuning the VDI calibration source (see Section 2) in steps of 10 GHz from 130 GHz. For each frequency measurement the calibration source was modulated at a period of 1 second with a sinusoidal profile, and the TES signal was demodulated in post processing. QUBIC-TD was configured to point at an elevation angle of $35°$ and to scan across azimuth at a constant rate from $-25°$ to $+25°$. The elevation angle was then increased by $0.2°$ and a new azimuth scan at constant rate was done in the reverse direction from $+25°$ to $-25°$. Each azimuth scan takes nearly 8 minutes, and an entire beam map at a given frequency is completed in 22 hours and 30 minutes. This matches well with the cryogenic hold time of the cryostat. The entire beam map measurement was preprogrammed in a script executed by the QUBIC instrument control software `QubicStudio`.

The result of the beam mapping measurement campaign is a series of maps for each TES pixel in the detector array. This is 244 maps for each frequency for a total of 1220 maps. Figure 18 shows example maps for TES#93 (ASIC 1) at three frequencies. The main lobe and secondary lobes are clearly visible and match well with theory.
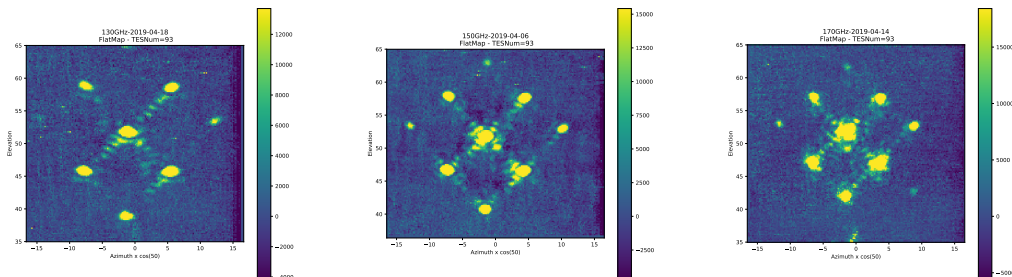

Figure 18. Maps of the synthetic beam for TES#93 (ASIC 1). The multilobe synthetic beam is shown here for 130 GHz, 150 GHz, and 170 GHz. An animated version of this plot with comparison to simulation can be viewed online at https://box.in2p3.fr/index.php/s/bzPYfmtjQW4wCGj

The secondary lobe locations depend on frequency while the main lobe is always at the same place. Figure 19 shows a cut across the beam maps of Figure 18. The secondary lobes are closer to centre as frequency increases, as expected. This is a key feature of the bolometric interferometer which makes spectroscopic imaging possible.
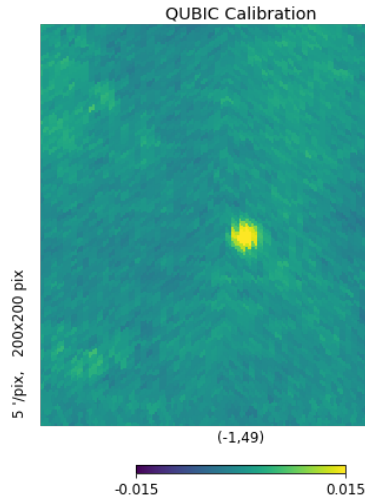
8 Map Making with Measured Synthesized Beams

Using the relative location and amplitude of all the peaks in the synthesized beam for each of the TES, we can now project the data onto the sky using optimal map-making to deconvolve from the effect of the multiple peaks. When observing the sky, this will result in an unbiased CMB map as has been shown using simulations [see 8, in this series of papers]. We have performed this with the calibration data in order to obtain an image of the point-like calibration source we have been using. The resulting image is shown in Figure 20 exhibiting the expected point-source shape with a FWHM of 0.68 degree in excellent agreement with expectations.
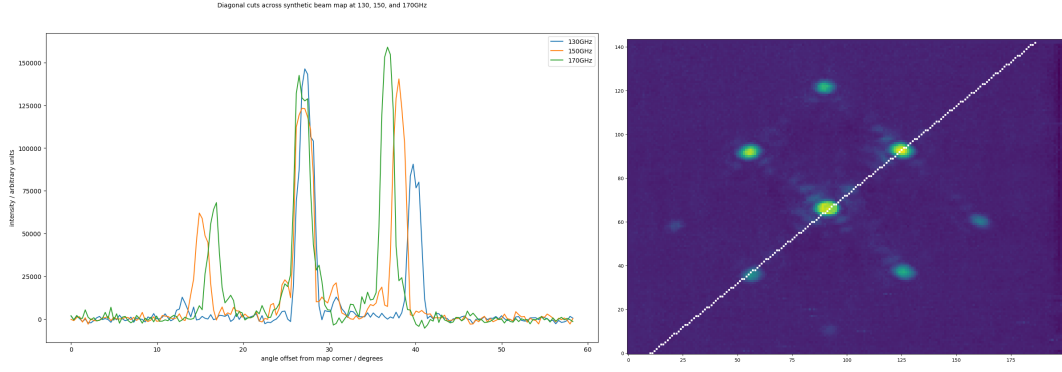
Figure 19. A cut across the synthetic beam maps shown in Figure 18. The plot on the left shows the coincident central lobe for each frequency and the secondary lobes which are closer to centre as frequency increases. The image on the right indicates the orientation of the slice.

The successful mapmaking with the measured synthesized beam is effectively an end-to-end checkout of the entire QUBIC system. In order for this exercise to be possible, all subsystems, interfaces between subsystems, and all associated software must be functioning correctly. This includes scientific and housekeeping data acquisition, telescope pointing control, and control and synchronisation of all subsystems. The software needed to make this measurement includes the system control software, the data acquisition software, data archiving and reading, and finally data analysis software together with comparison to system simulation software. The resulting map of Figure 20 shows that all subsystems are functioning correctly, and all subsystems are correctly managed and synchronized together into the overall system.

Figure 20. Calibration data with the source at 150 GHz projected on the sky using our map-making software to deconvolve from the multiple peaked synthesized beam. Small residuals of the deconvolved multiple peaks can be seen and are due to unmodeled non-linearity of the detectors due to saturation with the strong calibration source.

9 Conclusion

QUBIC underwent a long campaign of testing in the laboratory at APC in Paris. These measurements confirm that Bolometric Interferometry is a viable method for the measure of CMB B-mode polarization. In particular, using an artificial millimetre-wave source in the telescope far-field, a number of fundamental requirements were successfully demonstrated. The measured synthesized beam matches well with theory, and demonstrates that spectral imaging is possible. The spectral response matches the expected bandpass given the optical components in the optical chain. The polarization performance has less than 0.2% cross polarization contamination at 150 GHz which will make QUBIC the best instrument for polarization purity among the currently running CMB B-mode experiments.

The emphasis on QUBIC design has been on the suppression and control of systematic effects. QUBIC employs bolometric interferometry and a conservative polarization optical design which together has the advantage of exquisite control of systematics while still giving the high sensitivity inherent in the use of wide band bolometers.

Deployment of QUBIC on the scientific site of Alto Chorillo at 5000 m altitude in Argentina is expected during 2020. QUBIC will provide an extremely clean polarization map of the sky and together with spectro imaging, will have excellent separation of foreground sources.

Acknowledgments

References

[1] W. Hu and M. White, "A CMB polarization primer," *New Astron. Reviews*, vol. 2, pp. 323–344, Oct 1997.

[2] J. Aumont *et al.*, "QUBIC Technical Design Report," *arXiv e-prints*, p. arXiv:1609.04372, Sep 2016.

[3] C. O'Sullivan, M. De Petris, *et al.*, "QUBIC VIII: Optical design and performance," *arXiv e-prints*, p. arXiv:2008.10119, Aug. 2020.

[4] S. Masi *et al.*, "QUBIC V: Cryogenic system design and performance," *arXiv e-prints*, p. arXiv:2008.10659, Aug. 2020.

[5] M. Piat, G. Stankowiak, *et al.*, "QUBIC – IV: Performance of TES Bolometers and Readout Electronics," *J. Cosmo. Astroparticle Phys.*, vol. ?, p. ?, Oct 2020. to be submitted.

[6] M. A. Bigot-Sazy, R. Charlassier, J. C. Hamilton, J. Kaplan, and G. Zahariade, "Self-calibration: an efficient method to control systematic effects in bolometric interferometry," *A&A*, vol. 550, p. A59, Feb 2013.

[7] J.-C. Hamilton *et al.*, "QUBIC – I: Overview and Science Program," *J. Cosmo. Astroparticle Phys.*, vol. ?, p. ?, Oct 2020. to be submitted.

[8] L. Mousset, M. Gamboa, *et al.*, "QUBIC – II: Spectral Imaging," *J. Cosmo. Astroparticle Phys.*, vol. ?, p. ?, Oct 2020. to be submitted.

[9] J. A. Högbom, "Aperture Synthesis with a Non-Regular Distribution of Interferometer Baselines," *A&AS*, vol. 15, p. 417, Jun 1974.

[10] D. N. Fort and H. K. C. Yee, "A Method of Obtaining Brightness Distributions from Long Baseline Interferometry," *A&A*, vol. 50, p. 19, Jul 1976.

[11] A. C. S. Readhead and P. N. Wilkinson, "The mapping of compact radio sources from VLBI data.," *ApJ*, vol. 223, pp. 25–36, Jul 1978.

[12] T. J. Cornwell and P. N. Wilkinson, "A new method for making maps with unstable radio interferometers," *MNRAS*, vol. 196, pp. 1067–1086, Sep 1981.

[13] T. J. Pearson and A. C. S. Readhead, "Image Formation by Self-Calibration in Radio Astronomy," *Ann. Rev. Astron. Astrophys.*, vol. 22, pp. 97–130, Jan 1984.

[14] T. Cornwell and E. B. Fomalont, "Self-Calibration," in *Synthesis Imaging in Radio Astronomy II* (G. B. Taylor, C. L. Carilli, and R. A. Perley, eds.), vol. 180 of *Astronomical Society of the Pacific Conference Series*, p. 187, Jan 1999.

[15] F. Cavaliere, A. Mennella, M. Zannoni, *et al.*, "QUBIC VII: The feedhorn-switches system of the technological demonstrator," *J. Cosmo. Astroparticle Phys.*, vol. ?, p. ?, Oct 2020. to be submitted.